Sandoval-Santana, Juan Carlos; Zamora-Zamora, Roberto; Paredes, Rosario; Romero-Rochín, Victor

Intrinsic decoherence and recurrences in a large ferromagnetic f = 1 spinor bose–einstein condensate

Published in:
SYMMETRY

DOI:
10.3390/sym13010067

Published: 01/01/2021

Document Version
Publisher's PDF, also known as Version of record

symmetry

MDPI

Article

Intrinsic Decoherence and Recurrences in a Large Ferromagnetic $F = 1$ Spinor Bose–Einstein Condensate

Juan Carlos Sandoval-Santana [1,†,‡], Roberto Zamora-Zamora [2], Rosario Paredes [1,‡] and Victor Romero-Rochín [1,*,‡]

1 Instituto de Física, Universidad Nacional Autónoma de México, Apartado Postal 20-364, Ciudad de México 01000, Mexico; jcss.pms@gmail.com (J.C.S.-S.); rosario@fisica.unam.mx (R.P.)
2 Department of Applied Physics, QCD Labs, COMP Centre of Excellence, Aalto University, P.O. Box 13500, FI-00076 Aalto, Finland; roberto.zamorazamora@aalto.fi
* Correspondence: romero@fisica.unam.mx
† Current address: Departamento de Ciencias Básicas, Universidad Autónoma Metropolitana Azcapotzalco, Av. San Pablo 180, Col. Reynosa Tamaulipas, Ciudad de México 02200, Mexico.
‡ These authors contributed equally to this work.

Abstract: Decoherence with recurrences appear in the dynamics of the one-body density matrix of an $F = 1$ spinor Bose–Einstein condensate, initially prepared in coherent states, in the presence of an external uniform magnetic field and within the single mode approximation. The phenomenon emerges as a many-body effect of the interplay of the quadratic Zeeman effect, which breaks the rotational symmetry, and the spin-spin interactions. By performing full quantum diagonalizations, a very accurate time evolution of large condensates is analyzed, leading to heuristic analytic expressions for the time dependence of the one-body density matrix, in the weak and strong interacting regimes, for initial coherent states. We are able to find accurate analytical expressions for both the decoherence and the recurrence times, in terms of the number of atoms and strength parameters, which show remarkable differences depending on the strength of the spin-spin interactions. The features of the stationary states in both regimes are also investigated. We discuss the nature of these limits in light of the thermodynamic limit.

Keywords: Bose–Einstein condensates; quantum decoherence; full quantum dynamics

Citation: Sandoval-Santana, J.C.; Zamora-Zamora, R.; Paredes, R.; Romero-Rochín, V. Intrinsic Decoherence and Recurrences in a Large Ferromagnetic $F = 1$ Spinor Bose–Einstein Condensate. *Symmetry* **2021**, *13*, 67. https://doi.org/10.3390/sym13010067

Received: 7 November 2020
Accepted: 27 December 2020
Published: 31 December 2020

1. Introduction

The observation of stationarity in quantum systems relies on the existence of pairwise collisions in large conglomerates of atoms, either in an isolated environment or in contact with a larger environment [1–10]. While in the former case, the process through which the system reaches the stationary state may be termed intrinsic decoherence [11,12], in the latter case, it is simply known as decoherence. In reality, since one can consider the system (S) under study and the environment (R) as a composite closed system $(S + R)$, their time evolution is always unitary, and the observation of decoherence always refers to reduced quantities, namely observables of much fewer degrees of freedom of the total ones of the isolated system, say $N_S \ll N_R$, with N the number of degrees of freedom. Therefore, when studying a system in contact with a reservoir, one deals with the reduced density matrix of the former, ρ_S, integrating out the environment. This leads typically to master equations for the reduced density matrix of the system that has already ingrained the decoherence effects induced by the interaction with the environment [2,5,6,8–10]. In general, decoherence and recurrence phenomena have been widely studied both experimentally and theoretically. On the experimental side, some examples are the dephasing in interference fringes measured in condensates, the decay of laser-induced polarization in spectroscopic experiments [13,14], the amplitude damping in qudit photonic states [15], and the decoherence induced in single molecule junctions [16], among others. Measurements of purity have also been used to search for quantum coherence loss [17].

On the other hand, if the system under study is a large one, $N \gg 1$, but isolated from any environment, even though the evolution is always unitary, the system relaxes or decoheres to a stationary state [18] within a quantifiable decoherence time, in the sense that expectation values of one-body observables, such as temperature, magnetization, and, say, few-body correlations, behave as if the full system had relaxed to a stationary state for times longer than the decoherence time. If the system is finite, there appear recurrences or revivals of states near the initial one, but in typical systems, the recurrence time may grow with no bound in the thermodynamic limit $N \to \infty$. The behavior of those few-body properties can be directly studied solely with their corresponding reduced few-body density matrices, whose time evolution is no longer unitary within their reduced Hilbert space. It is of interest for our purposes that the experiments in ultracold gases showing Bose–Einstein condensation [19–22] are the closest to dealing with true isolated systems. Yet, these gases, due to atomic collisions, relax to equilibrium and, when in the presence of external magnetic fields, show decoherence phenomena [23,24]. The study of the magnetization of the latter case is the subject of the present article. Hence, to be specific, we call intrinsic decoherence that of the few-body properties, in an otherwise very large isolated system. Recurrences are not observed in the ultracold gases since unwanted processes, such as three-body collisions, make the thermal state unstable in a relatively short time [25]. An interesting question concerns the nature of the stationary state and the inquiry of whether it is a thermal state or not. In this regard, the essence of the Eigenstate Thermal Hypothesis (ETH) [26–30] is to establish that the thermodynamic properties of few-body observables are contained in the eigenstate closest to the equilibrium average energy. Hence, a simple test is to compare the few-body density matrices of the stationary state of the actual unitarily evolving state with those of the energy eigenstate with an energy similar to the mean of the state evolving in time. Deviations from this typical behavior, such as the many-body localization phenomenon [31], are also of current interest. In light of these observations, we advance here that depending on the two-body interaction strength in an $F = 1$ Spinor Bose–Einstein Condensate (SBEC) in the presence of external homogeneous magnetic fields, we observe intrinsic decoherence of the magnetization, but with different features leading to both typical and non-typical stationary states.

To be precise, within a full quantum scheme, we study here the phenomenon of intrinsic decoherence, as well as the appearance of recurrences, in the time dynamics of an $F = 1$ Spinor Bose–Einstein Condensate (SBEC) composed of a mixture of three different hyperfine spin components, in the presence of a uniform magnetic field, starting in a well-defined coherent state. Depending on the sign of the spin-mixing interaction strength, the atomic cloud can be polar if positive, such as a gas of ^{23}Na atoms, or ferromagnetic if negative, as in a gas of ^{87}Rb atoms [32,33]. We shall study here the ferromagnetic case only since the condensate acquires a macroscopic spin texture that makes it behave as a "giant" spin. It is worth mentioning that the system we address is very similar to the recent experimental investigation on the spin dynamics of an $F = 1$ ^{87}Rb spinor macroscopic condensate, where use of the SBEC as a sensible magnetometer is explored [24]. The present model has also been used to study quantum phase transitions in space [34]. The dynamics of the spin mixture is followed in the presence of the external magnetic field, which gives rise to linear and quadratic Zeeman contributions, with strengths p and q, which together with the interaction term, of strength η, give rise to the phenomena herein analyzed.

Since we are able to very accurately diagonalize the Hamiltonian of the system up to $N \sim 10^4$ atoms, we can study the dynamics of any initial state and then calculate reduced density matrices of few-bodies. Here, we analyze the one-body density matrix for a full family of coherent states, as one expects them to be the most resilient to the spin interaction, clearly showing Larmor-like oscillations in the expectation value of the measurable spin (or magnetization) one-body observable. We point out that coherent states are usually expected to yield the closest to the quasi-classical dynamics of the magnetization, in a mean-field fashion, with little or no decoherence [35]. Indeed, if there is no quadratic Zeeman coupling, the coherent states show no signs of decoherence, but as soon as the

full rotational symmetry is broken by the presence of such a coupling, this, in conjunction with the natural two-body collisions, yields the decoherence or collapse of the very definite Larmor oscillations generated by the presence of the external field. Due to the finite number of atoms and the relatively small Hilbert space size, the oscillations recur or revive after longer periods of time, to decohere again. After a long set of calculations, we are able to find out three clear regimes depending on the value of the dimensionless parameter $N|\eta|/q$, a weak interacting one $N|\eta|/q \ll 1$, a strong one $N|\eta|/q \gg 1$, and a crossover $N|\eta|/q \sim 1$, in which, although all show decoherences and recurrences, their dependence on the parameters q and η and especially on N, as well as the nature of their corresponding stationary states are very different. Furthermore and very importantly, after the mentioned numerical study and with the insight of the analytic solution to the non-linear single mode model [36,37], we are able to heuristically deduce analytic expressions for the full one-body density matrix in the weak and strong interacting regimes. These expressions are certainly the leading order contributions of the full unknown analytical solution and show a remarkable agreement with the predictions of the full quantum numerical solution. We are thus able to provide analytical expressions for the recurrence and decoherence times in terms of the parameters q, η, and N and their dependence on the particular initial states. We also highlight the fact that the strong interaction regime shows a "typical" behavior of a macroscopic system since the decoherence and recurrence times show an expected dependence on N, in the sense that as $N \to \infty$, the recurrence time grows with no bound, thus making the quasistationary state closer to a true one. In addition, the nature of the stationary state behaves similarly to the ETH as it has the same reduced one-body density matrix as the eigenstate whose energy equals the gas average energy.

This manuscript is organized into five sections. In Section 2, we introduce the model Hamiltonian that describes the spinor BEC within the Single Mode Approximation (SMA) and discuss how we are able to accurately obtain its full quantum diagonalization. In Section 3, we introduce the one-body density matrix and its time evolution for a family of coherent states in the ferromagnetic case, preparing the stage for Section 4, which shows our main contributions regarding the discussion of decoherence recurrences in the weak and strong interacting regimes. Finally, a discussion and a summary of this work are presented in Section 5.

2. An $F = 1$ SBEC within the SMA Approximation—Full Quantum Diagonalization

The many-body $F = 1$ SBEC Hamiltonian with linear and quadratic Zeeman couplings to an external homogeneous magnetic field $\vec{B}$, within the contact approximation, is:

$$\begin{aligned}\mathcal{H} &= \int d\mathbf{r}\left(\frac{\hbar^2}{2m}\nabla\hat{\psi}^\dagger_\alpha(\mathbf{r})\cdot\nabla\hat{\psi}_\alpha(\mathbf{r}) + U(\mathbf{r})\hat{\psi}^\dagger_\alpha(\mathbf{r})\hat{\psi}_\alpha(\mathbf{r}) + \frac{c_0}{2}\hat{\psi}^\dagger_\alpha(\mathbf{r})\hat{\psi}^\dagger_\beta(\mathbf{r})\hat{\psi}_\beta(\mathbf{r})\hat{\psi}_\alpha(\mathbf{r})\right.\\ &\quad + \frac{c_2}{2}\hat{\psi}^\dagger_\alpha(\mathbf{r})\hat{\psi}^\dagger_{\alpha'}(\mathbf{r})\mathbf{F}_{\alpha\beta}\cdot\mathbf{F}_{\alpha'\beta'}\hat{\psi}_\beta(\mathbf{r})\hat{\psi}_{\beta'}(\mathbf{r}) + \tilde{p}\hat{\psi}^\dagger_\alpha(\mathbf{r})\left[\vec{B}\cdot\mathbf{F}\right]_{\alpha\beta}\hat{\psi}_\beta(\mathbf{r})\\ &\quad \left. + \tilde{q}\hat{\psi}^\dagger_\alpha(\mathbf{r})\left[\vec{B}\cdot\mathbf{F}\right]_{\alpha\alpha'}\left[\vec{B}\cdot\mathbf{F}\right]_{\alpha'\beta}\hat{\psi}_\beta(\mathbf{r})\right)\end{aligned} \tag{1}$$

where $\hat{\psi}_\alpha(\mathbf{r})$ are the annihilation operators of particles at $\mathbf{r}$ with spin $\alpha = -1, 0, +1$ and $\mathbf{F}_{\alpha\beta}$ are the $F = 1$ angular momentum matrices. c_0 and c_2 are interaction coefficients proportional to the corresponding s-wave scattering lengths. If $c_0 > c_2$, the system is polar and for $c_0 > c_2$, ferromagnetic [32]. $U(\mathbf{r})$ is an external confining potential, typically harmonic. In general, the field operator is given by:

$$\hat{\psi}_\alpha(\mathbf{r}) = \sum_m \phi_{m\alpha}(\vec{r})\hat{b}_{m\alpha} \tag{2}$$

where $\phi_{m\alpha}(\vec{r})$ are elements of the basis of the one-particle Hilbert space and $\hat{b}_{m\alpha}$ the corresponding creation operators. For ultracold gases, a usual approximation is to consider a self-consistent, to be determined, ground state wavefunction only $\Psi_{0\alpha}(\mathbf{r}, t)$, such that

$\hat{\psi}_\alpha(\mathbf{r},t) \approx \Psi_{0\alpha}(\mathbf{r},t)\hat{b}_0$, that is all spin states are in the same ground state. This leads to a set of three coupled Gross–Pitaevskii (GP) equations [32,33]. These can be solved numerically, and as shown in Figure 1, the solution for a homogenous magnetic field shows that the spatial part is unaffected by the presence of such a field, showing Larmor-like oscillations of the magnetization; see below. That is, the dynamics occurs only in the spin degrees of freedom, and it is not transferred to spatial excitations such as phonons and vortices. This would not be so if the external field were inhomogeneous [38]. The previous observations indicate that a single mode approximation can be made at the level of the GP description (SMA-GP), that is an assumption that the ground state wavefunction is the same for all spin components α. Therefore, if we set $\Psi_{0\alpha}(\mathbf{r},t) = \psi_0(\vec{r})\zeta_\alpha(t)$ with $\zeta_\alpha(t)$ a simple three-component spinor, we can integrate out the spatial part and find very simple dynamical equations, called SMA-GP (not shown here), for the time evolution of $\zeta(t)$. The result of those is shown also in Figure 1 where we plot the time evolution of the magnetization $\vec{f}(t) = \int d\mathbf{r}\Psi^*_{0\alpha}(\mathbf{r},t)\mathbf{F}_{\alpha\beta}\Psi^*_{0\alpha}(\mathbf{r},t)$ with full 3D GP (see [39] for the details of our methods), and $\vec{f}(t) = \zeta^*_\alpha(t)\mathbf{F}_{\alpha\beta}\zeta^*_\alpha(t)$ with the SMA-GP equations. The agreement is essentially perfect. The unphysical feature of the SMA-GP equations, as well as of the full 3D GP is that they are incapable of showing decoherence effects. This is not surprising since GP equations assume that there is a single macroscopic wavefunction for the ground state even in the presence of dynamical effects.

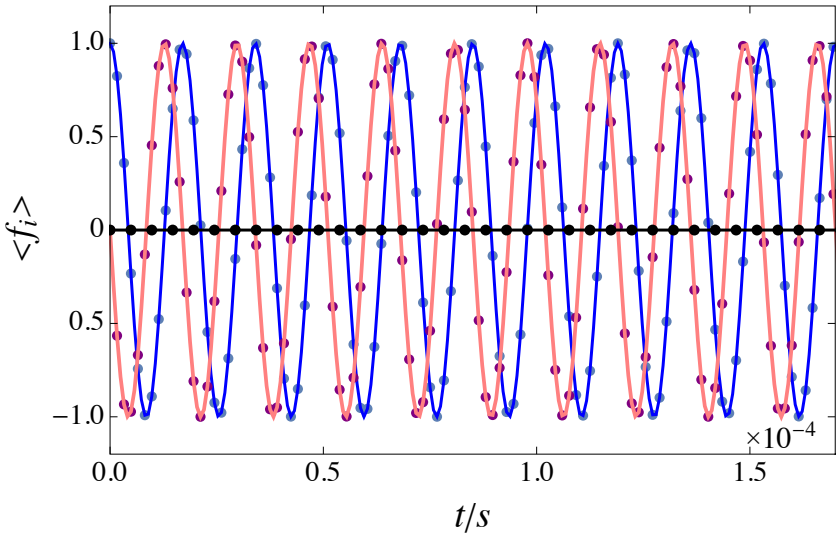

Figure 1. Magnetization $\vec{f}$ as a function of time t. Comparison of a full 3D Gross–Pitaevskii (dotted line) versus Single Mode Approximation (SMA)-Gross–Pitaevskii (GP) calculations (continuous line), for a ^{87}Rb $F = 1$ ferromagnetic Spinor Bose–Einstein Condensate (SBEC). Blue and red lines are the x- and y-components, with black the z-component. We use ^{87}Rb constants and experimentally accessible fields, $\tilde{p} = -0.7h$ MHz G^{-1}, $\tilde{q} = 72h$ Hz G^{-2}, $c_0 = 50.2$ Å, $c_2 = 50.9$ Å with a field $B_z = 84$ mG and for $N = 6.8 \times 10^4$ atoms.

The above results motivate, and partially justify, a radical SMA that assumes that the field operator can be written as $\hat{\psi}_\alpha(\mathbf{r}) \approx \Psi_0(\mathbf{r})\hat{a}_\alpha$, such that the spatial part can be integrated out and we can deal with the spin part in full. That is, the many-body aspects of the spin part can be fully taken into account. This will lead, as is the purpose of this paper, to showing quantifiable aspects of intrinsic decoherence, as explained above and the recurrence or revivals of the predictable oscillations for initial coherent states. The SMA approximation leads to a seemingly simple Hamiltonian for an $F = 1$ SBEC [40–43]:

$$\hat{H} = p\hat{f}_z + q\hat{Q} + \eta\hat{f}^2. \tag{3}$$

Within SMA, this Hamiltonian differs from that of Equation (1) by a term proportional to the number operator $\hat{N}$, which commutes with $\hat{H}$. The first and second terms represent the linear and quadratic Zeeman contributions, $p \sim \tilde{p}B$, $q \sim \tilde{q}B^2$, while the third one is the spin-mixing interaction, $\eta \sim (c_2 - c_0)$, such that $\eta > 0$ is polar and $\eta < 0$ ferromagnetic [32]. As described in the Introduction, our interest here is the ferromagnetic case. From now on, our goal is the study of Hamiltonian $\hat{H}$ and its ensuing dynamics; therefore, we shall vary all three parameters independently in order to elucidate their role in the dynamics. These parameters can certainly be tuned experimentally. The above operators in $\hat{H}$ are given in terms of the creation and annihilation operators of bosonic atoms in the z-direction spin states $+1$, 0, and -1, in obvious notation,

$$\begin{aligned} \hat{f}_z &= \hat{a}^\dagger_{+1}\hat{a}_{+1} - \hat{a}^\dagger_{-1}\hat{a}_{-1} \\ \hat{Q} &= \hat{a}^\dagger_{+1}\hat{a}_{+1} + \hat{a}^\dagger_{-1}\hat{a}_{-1} \\ \hat{f}^2 &= \hat{T}^\dagger + \hat{T} + (2\hat{a}^\dagger_0\hat{a}_0 - 1)\hat{Q} + \hat{f}_z^2 \end{aligned} \tag{4}$$

where:

$$\hat{T} = 2\hat{a}^\dagger_{-1}\hat{a}^\dagger_{+1}\hat{a}_0\hat{a}_0. \tag{5}$$

Certainly, $\hat{\vec{f}} = (\hat{f}_x, \hat{f}_y, \hat{f}_z)$ is the one-body spin or magnetization vector operator, with:

$$\begin{aligned} \hat{f}_x &= \frac{1}{\sqrt{2}}\Big(\hat{a}^\dagger_0(\hat{a}_{+1} + \hat{a}_{-1}) + (\hat{a}^\dagger_{+1} + \hat{a}^\dagger_{-1})\hat{a}_0\Big) \\ \hat{f}_y &= \frac{i}{\sqrt{2}}\Big(\hat{a}^\dagger_0(\hat{a}_{+1} - \hat{a}_{-1}) - (\hat{a}^\dagger_{+1} - \hat{a}^\dagger_{-1})\hat{a}_0\Big) \end{aligned} \tag{6}$$

and $\hat{f}^2 = \hat{f}_x^2 + \hat{f}_y^2 + \hat{f}_z^2$, whose expectation value is the magnetization or spin texture. Introducing the spin state number operators $\hat{n}_\sigma = \hat{a}^\dagger_\sigma\hat{a}_\sigma$, one can also write $\hat{f}_z = \hat{n}_{+1} - \hat{n}_{-1}$ and $\hat{Q} = \hat{n}_{+1} + \hat{n}_{-1}$, forms that can be useful in interpreting our results below.

For a given number of atoms N, the size of the Hilbert space is $\Omega = (N+1)(N+2)/2$, and therefore, the size of Hamiltonian given by Equation (3) scales as $\sim N^2 \times N^2$. In order to find the time evolution of the system, we have to diagonalize the Hamiltonian, a difficult task that can be eased by exploiting its symmetries. Obviously, the total number operator $\hat{N} = \hat{n}_{+1} + \hat{n}_0 + \hat{n}_{-1}$ commutes with the Hamiltonian $\hat{H}$. In addition, due to its Lie structure, it is easy to show that $\left[\hat{f}_z, \hat{H}\right] = 0$. Hence, instead of using the "natural" basis of number occupation $|n_{+1}, n_0, n_{-1}\rangle$, in obvious notation, one finds a better alternative to use $|M, n_0\rangle$, with $M = n_{+1} - n_{-1}$ the eigenvalues of $\hat{f}_z$, with values $-N, -N+1, \ldots, N-1, N$. Atom number conservation $N = n_{+1} + n_0 + n_{-1}$ yields the third quantum number, obviated in the state labels. In this basis, the Hamiltonian is block diagonal in M, and the matrix elements show simple expressions,

$$\langle M', n_0'|\hat{f}_z|M, n_0\rangle = M\delta_{M'M}\delta_{n_0'n_0}\,, \tag{7}$$

$$\langle M', n_0'|\hat{Q}|M, n_0\rangle = (N - n_0)\delta_{M'M}\delta_{n_0'n_0}\,, \tag{8}$$

$$\begin{aligned} \langle M', n_0'|\hat{f}^2|M, n_0\rangle &= 2\sqrt{(n_{-1}+1)(n_{-1}+1)n_0(n_0-1)}\,\delta_{M'M}\delta_{n_0'(n_0-2)} \\ &+ 2\sqrt{n_{+1}n_{-1}(n_0+1)(n_0+2)}\,\delta_{M'M}\delta_{n_0'(n_0+2)} \\ &+ (2n_0 - 1)(N - n_0)\delta_{M'M}\delta_{n_0'(n_0+2)} + M^2\delta_{M'M}\delta_{n_0'n_0}\,, \end{aligned} \tag{9}$$

where $n_{+1} = (N + M - n_0)/2$ and $n_{-1} = (N - M - n_0)/2$. We note that the matrix elements in Equations (7)–(9) do not link blocks with different values of M; however,

they connect different matrix elements with jumps of two for n_0. Then, the Hamiltonian H can be diagonalized and written as,

$$\hat{H}|M, m_M\rangle = E_{M,m_M}|M, m_M\rangle \tag{10}$$

where, for each block M, $m_M = 1, 2, \ldots, m_M^{\max}$, and $m_M^{\max} = (N - |M| + 1)/2$ or $m_M^{\max} = (N - |M| + 2)/2$ if M is odd or even, respectively. This analysis can also be applied to SBEC with $F > 1$ [44,45]. The block-diagonal structure of the Hamiltonian given by Equation (3) allows not only very accurate calculation of the energy eigenvectors and eigenvalues for values up to $N \sim 10^4$, as given by Equation (10), but also implementing full quantum evolution of any initial quantum state for arbitrary values of time. For this, we perform numerically exact diagonalization block-by-block using pyCUDA linear algebra routines, in a server with an eight CPU core, 128 GB RAM, and with the graphic card Nvidia Tesla C2075. Since this diagonalization can be obtained for a wide variety of parameters, the ensuing time evolutions we obtain do not suffer from the accumulation of errors, thus maintaining the same numerical precision at any time step. Depending on the value of N and the needed time steps, the full evolution of a given initial state elapsed between a few GPU seconds up to several hours. As an example that is easy to visualize, in Figure 2, we display the Hamiltonian structure for $N = 6$ particles with a Hilbert space size of 28, each blue square representing a block of magnetization M, whose size is given below. The intensity of the color blue and the size of the blocks depend on the value of M. Although we do not address it here, we show in Figure 3 the spectra and their degeneracy for different values of p, q, and η for $N = 10^3$, to illustrate its richness. All the figures below are in dimensionless units. Since the three parameters of Hamiltonian $\hat{H}$ all have units of energy, for the ease of varying all parameters without worrying about unit adjustments in different cases, we assume a unit of energy ϵ_0, such that the three parameters are adimensionalized with it and time is adimensionalized as $\tau = \epsilon_0 t/\hbar$.

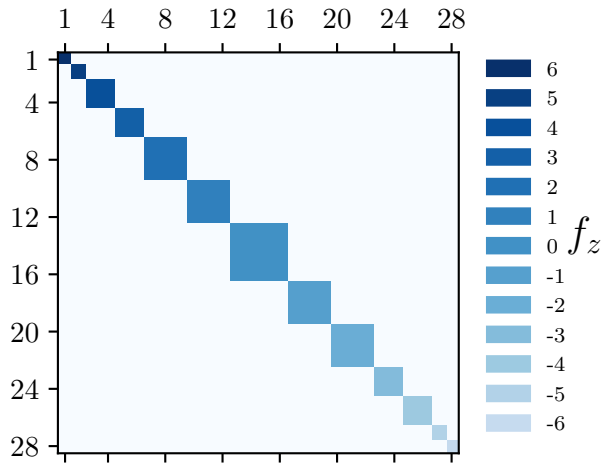

Figure 2. Hamiltonian structure for N = 6 particles where the Hilbert space size is 28, each blue square representing a block of magnetization M. The intensity of the color blue and the size of the blocks depend on the value of M.

Despite the fact that $\hat{f}_z$ and $\hat{Q}$ commute, the interesting and rich behavior of this model arises because of the non-commutativity of the quadratic Zeeman term $\sim\hat{Q}$ and the spin interaction $\sim\hat{f}^2$. Further, in the absence of the quadratic Zeeman interaction, $q = 0$, the Hamiltonian can be analytically diagonalized both for $F = 1$ [46] and $F = 2$ [44]. The presence of the quadratic term, $q \neq 0$, breaks the axisymmetry [40], and this system becomes an excellent one to study quantum phase transition [47], quench-dynamical behaviors [48], the quantum Kibble–Zurek mechanism [49], and spin fragmentation [43], among other mechanisms. On the contrary, if there is no atomic interactions, $\eta = 0$,

the problem is also trivial and right away diagonal, as given by Equations (7)–(9). Hence, reiterating, the presence of the atomic interactions is mediated by the presence of the Zeeman quadratic term.

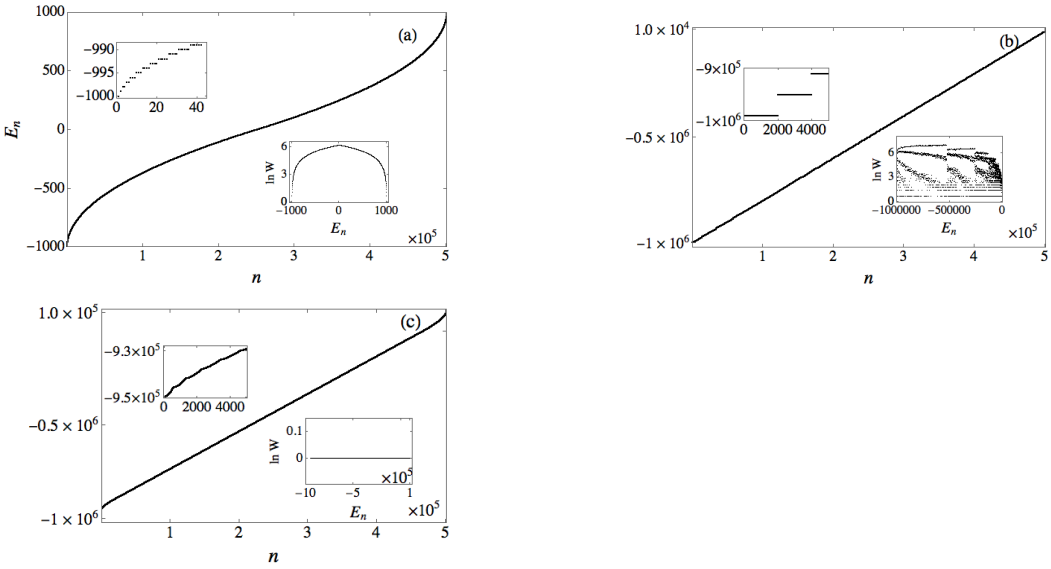

Figure 3. Energy spectrum E_n and its degeneracy $\ln W$ (right inset), for $N = 10^3$ particles and (**a**) $p = 1$, $q = 0$, and $\eta = 0$; (**b**) $p = 0$, $q = 0$, and $\eta = -1$; and (**c**) $p = 1$, $q = 100$, and $\eta = -1$. In the left inset, we show the detail of the energy spectrum.

3. Time Evolution of the One-Body Density Matrix in Coherent States

With the full quantum diagonalization described above, we can calculate the time evolution of arbitrary initial states $|\Psi_0\rangle$. Here, we will concentrate on a family of initial coherent states, introduced below. For this purpose, we briefly mention that, as expected, the time evolution can also be performed by blocks in the following manner. First, since the unitary propagator operator can be written as,

$$\mathbf{U}(t,t_0) = \sum_{M=-N}^{N} \sum_{m=1}^{m_M \max} e^{-\frac{i}{\hbar} E_{M,m_M}(t-t_0)} |M,m_M\rangle\langle M,m_M| \,, \tag{11}$$

one just needs the overlaps $\langle M,m_M|\Psi_0\rangle$ to find the time evolution of any $|\Psi_0\rangle$. However, since many of the usual physical quantities are typically one- or two-body operators, we shall devote our attention to the one-body density matrix, which allows for calculating all the statistical properties of all one-body operators, such as the matrices $\hat{f}_x$, $\hat{f}_y$, and $\hat{f}_z$. For this, we note that since any one-body operator can be written as,

$$\hat{\mathcal{O}}^{(1)} = \sum_{kj} \mathcal{O}_{ij} \hat{a}_k^\dagger \hat{a}_j \tag{12}$$

with k and j taking the values $+1$, 0, and -1 and $\mathcal{O}_{ij}$ complex numbers, the expectation value of any operator $\hat{\mathcal{O}}^{(1)}$ requires the knowledge of the expectation values of the operators $a_k^\dagger a_j$ for all values of kj. These expectation values are those of the one-body density matrix. Explicitly, for a given initial state $|\Psi_0\rangle$, the one-body density matrix for all times is given by,

$$\rho_{jk}(t) = \frac{1}{N} \langle \Psi_0 | \mathbf{U}^\dagger(t,0) \hat{a}_k^\dagger \hat{a}_j \mathbf{U}(t,0) | \Psi_0 \rangle, \tag{13}$$

where the $1/N$ factor is introduced such that the trace of the reduced density is always unity. This yields in turn that the expectation values of spin operators are also bounded by one. Although we do not exploit it here, it is worth mentioning that if we limit ourselves

to one-body properties, one could also use the properties of the Gell–Mann spin one matrices [50]. A very interesting and useful property of the one-body density matrix given above, in the representation of the $\hat{a}_\alpha$, $\alpha = -1, 0, +1$ corresponding to the z-direction spin basis, is that the one-body reduced density matrix is diagonal in such a basis,

$$\rho_{jk}^{(s)} = \frac{1}{N}\langle M, m_M|\hat{a}_k^\dagger \hat{a}_k|M, m\rangle \delta_{jk}\,. \tag{14}$$

While we did not prove this result, we extensively verified it, and we believe it follows from the commutation of $\hat{f}_z$ with the Hamiltonian. The fact that the true stationary density matrix $\rho_{jk}^{(s)}$ is diagonal in this basis will greatly facilitate the elucidation of the (quasi)stationary states reached in the time evolution of an initial coherent state.

As we can accurately calculate the matrix $\rho_{kj}(t)$ for any time using Equation (13), we now turn our attention to the initial set of coherent states [35]:

$$|\theta, \varphi\rangle = \frac{1}{\sqrt{N!}}\left(\zeta_1 \hat{a}_1^\dagger + \zeta_2 \hat{a}_2^\dagger + \zeta_3 \hat{a}_3^\dagger\right)^N |0\rangle\,, \tag{15}$$

where $\zeta_1 = e^{-i\varphi}\cos\left(\frac{\theta}{2}\right)^2$, $\zeta_2 = \frac{\sin\theta}{\sqrt{2}}$ and $\zeta_3 = e^{i\varphi}\sin\left(\frac{\theta}{2}\right)^2$, with θ and φ the usual angles of the unit sphere and $|0\rangle$ denoting the vacuum state with no particles. Alternatively, a coherent state can also be written as,

$$|\theta, \varphi\rangle = e^{-i\varphi \hat{f}_z} e^{-i\theta \hat{f}_y}|N, 0, 0\rangle\,. \tag{16}$$

A very important property to take into account is that these coherent states are eigenstates of $\hat{f}^2$, that is $\hat{f}^2|\theta, \varphi\rangle = N(N-1)|\theta, \varphi\rangle$. We point out that the distribution of energy eigenstates in an arbitrary coherent state involve, in general, several if not many blocks of different values of the quantum number M. The main features of the time evolution of these states, as we amply discuss and show below, is that the elements of the one-body density matrix in these states show an initial oscillation that suffers intrinsic decoherence followed by a stationary state and revivals at later times, with this behavior being repeated ad infinitum. It is evident that both the decoherence and recurrence times depend on the p, q, and η parameters, as well as on the initial state (θ, ϕ), but an important issue is its dependence on N. As mentioned in the Introduction, we identified that the dependence on N is very different in two opposite limits $N|\eta|/q \ll 1$ and $q/N|\eta| \ll 1$, evidently called weak and strong interacting regimes.

Since one can show that the set of operators $\hat{f}_z$, $\hat{Q}$, and $\hat{f}^2$ is not part of a Lie algebra, the finding of an analytic expression for the reduced density matrix appears as a very difficult task. Nonetheless, the main contribution of this article is to show that the time evolution of the SBEC one-body properties can be summarized quite precisely with explicit (semi-)analytic expressions for the time evolution of the density matrix elements $\rho_{kj}(t)$, given in Equation (13), for an arbitrary initial coherent state such as Equation (15), in the weak and strong limits. These expressions, as well as their validity limits are found in a heuristic manner based on a very large number of precise numerical evaluations of time evolutions for a wide variety of values of the Hamiltonian parameters and for a collection of different initial coherent states.

In order to introduce our expressions for the one-body density matrix in the following section, we first discuss preliminary exact results. Note that the one-body density matrix $\rho_{jk}(t)$, given by (13), can be first expressed as,

$$\rho_{jk}(t) = \langle\theta|\mathbf{U}_{QI}^\dagger(t,0)a_k^\dagger a_j \mathbf{U}_{QI}(t,0)|\theta\rangle e^{i(j-k)(pt/\hbar+\varphi)} \tag{17}$$

where:

$$\mathbf{U}_{QI}(t,0) = e^{-i\left(q\hat{Q}+\eta\hat{f}^2\right)t/\hbar} \tag{18}$$

and $|\theta\rangle \equiv |\theta, 0\rangle$ is the coherent state for any value of θ and $\varphi = 0$. We see that for any initial state, the role of the $p\hat{f}_z$ term and the angle φ simply amount to a phase factor, while the whole dynamics is ruled by the quadratic Zeeman $q\hat{Q}$ and the interaction $\eta\hat{f}^2$ terms. Whether one term or the other dominates depends on the relative values of the strength parameters q and η. We further note that if $q = 0$, the interactions play no role since the coherent states are eigenstates of $\hat{f}^2$. Therefore, in order to observe the effect of both terms, both η and q must be nonzero.

As an illustration of the typical time evolution of coherent states, in Figure 4, we show sequences of decoherences and recurrences in the weak $N|\eta|/q \ll 1$, strong $q/N|\eta| \ll 1$, and crossover $N|\eta|/q \sim 1$ regimes. We found that in the extreme cases, the recurrences appear at periodic intervals, thus making feasible their prediction, while in the crossover, as the two effects contribute similarly, the sequences can be very irregular, and we make no attempt to analyze them here.

We would like to point out, as can be seen from Equation (17), that the time evolution of the one-body density matrix, being an expectation value, certainly depends on the initial state and on the Hamiltonian parameters, but also and very importantly, on the operator itself. Thus, the phenomenon shown in Figure 4, and their characteristic times analyzed in the sections below, cannot be explained based solely on the energy distribution in the initial state and on the properties of the energy spectra.

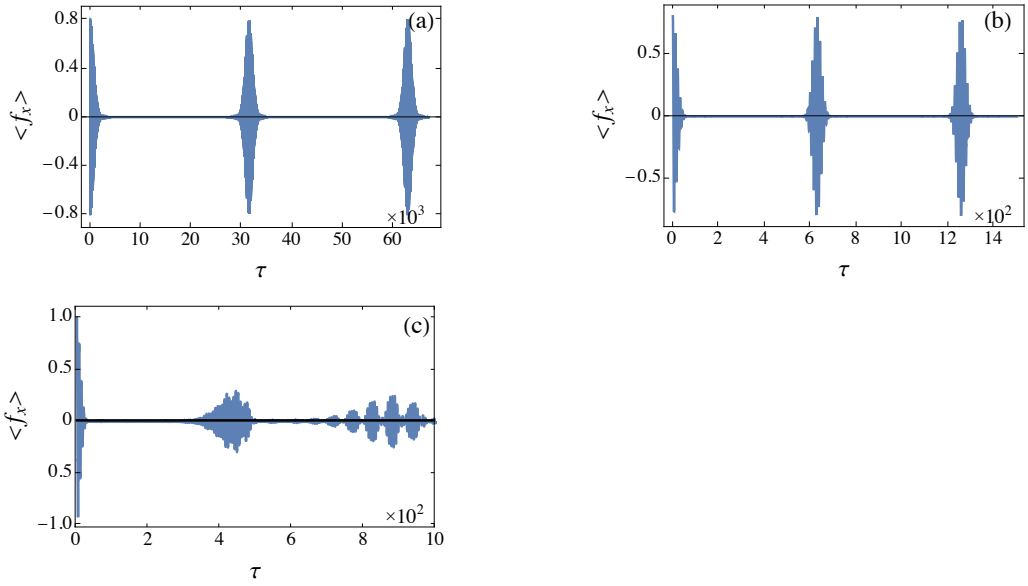

Figure 4. Time evolution of the expectation value $\langle \hat{f}_x \rangle$ illustrating the sequence of decoherences and recurrences; (**a**) weak interaction $N|\eta|/q \ll 1$ ($q = 1$, $\eta = -10^{-4}$, $\theta = 3\pi/10$); (**b**) strong interaction $q/N|\eta| \ll 1$ ($q = 1$, $\eta = -10^4$, $\theta = 3\pi/10$); and (**c**) crossover $q/N|\eta| \sim 1$ ($q = 1$, $\eta = -10^{-2}$, $\theta = \pi/2$). In all cases, $N = 100$.

4. Decoherence and Recurrences in the Strong and Weak Interacting Regimes

To proceed with the finding of the weak and strong interacting extremes, we note that the density matrix, Equation (17), can be written in two alternative forms,

$$\rho_{jk}(t) = \langle\theta| e_T^{-\frac{i}{\hbar}\eta\int_0^\tau \hat{V}_I(\tau)d\tau}\, a_k^\dagger a_j\, e_T^{\frac{i}{\hbar}\eta\int_0^\tau \hat{V}_I(\tau)d\tau} |\theta\rangle e^{i((k-j)pt/\hbar+\varphi)} e^{i\delta_{k,j\pm1}(\delta_{j,2}-\delta_{k,2})qt/\hbar} \tag{19}$$

or:

$$\rho_{jk}(t) = \langle\theta| e_T^{-\frac{i}{\hbar}q\int_0^\tau \hat{V}_Q(\tau)d\tau}\, a_k^\dagger a_j\, e_T^{\frac{i}{\hbar}q\int_0^\tau \hat{V}_Q(\tau)d\tau} |\theta\rangle e^{i((k-j)pt/\hbar+\varphi)}\,. \tag{20}$$

where:

$$\begin{aligned} \hat{V}_I(\tau) &= e^{iq\hat{Q}\tau/\hbar}\hat{f}^2 e^{-iq\hat{Q}\tau/\hbar} \\ \hat{V}_Q(\tau) &= e^{i\eta\hat{f}^2\tau/\hbar}\hat{Q}e^{-i\eta\hat{f}^2\tau/\hbar}\,, \end{aligned} \tag{21}$$

and e_T stands for the time-ordered exponential. The first form, Equation (19), is appropriate for the study of the weak interaction $N|\eta|/q \ll 1$, while the second one, Equation (20), for the strong one $q/N|\eta| \ll 1$. Note that the exact limits $\eta = 0$ and $q = 0$ are explicitly recovered in Equations (19) and (20).

In addition to the analysis of a large number of numerical calculations of the time evolution of coherent states, varying all the relevant parameters, we also used as insight the analytical solution of the non-linear single mode Hamiltonian $\hat{h} = -\mu\hat{a}^\dagger\hat{a} + u\hat{a}^\dagger\hat{a}^\dagger\hat{a}\hat{a}$ (see [36,37]) that for usual harmonic oscillator coherent states [51] shows collapses whose envelope is of a Gaussian shape followed by revivals, with characteristic times that depend exclusively on the state and the Hamiltonian parameters. Furthermore, the recurrences are observed to appear at periodic times. Based on this and on the numerical evidence, we proceed now to present the heuristic (semi-)analytic forms of the density matrix in the two extremes.

4.1. Strong Interaction Regime $q/N|\eta| \ll 1$

In this regime, the leading terms depend mostly on the quadratic Zeeman coupling q, and the one-body reduced density matrix can be very precisely fitted by the following form,

$$\rho_{jk}(t) \approx \rho_{jk}(0)e^{\frac{N}{2}\sin^2\theta\left[\cos\left(\frac{q(k-j)}{\hbar N}t\right)-1\right]}e^{i\cos\theta(k-j)qt/\hbar}e^{i(k-j)pt/\hbar} \quad j \neq k\,. \tag{22}$$

with $\rho_{jk}(0)$ given by,

$$\rho_{jk}(0) = \begin{pmatrix} \cos^4\frac{\theta}{2} & \frac{1}{\sqrt{2}}e^{i\varphi}\sin\theta\cos^2\frac{\theta}{2} & \frac{1}{4}e^{2i\varphi}\sin^2\theta \\ \frac{1}{\sqrt{2}}e^{-i\varphi}\sin\theta\cos^2\frac{\theta}{2} & \frac{1}{2}\sin^2\theta & \frac{1}{\sqrt{2}}e^{-i\varphi}\sin\theta\sin^2\frac{\theta}{2} \\ \frac{1}{4}e^{2i\varphi}\sin^2\theta & \frac{1}{\sqrt{2}}e^{i\varphi}\sin\theta\sin^2\frac{\theta}{2} & \sin^4\frac{\theta}{2} \end{pmatrix}. \tag{23}$$

which was obtained using the Lie algebra method [52].

From Equation (22), it can immediately be seen that the structure of periodic recurrences with decoherences in relatively shorter times than the former is given by the real exponential term $\exp(\frac{N}{2}\sin^2\theta\left[\cos\left(\frac{q(j-k)}{\hbar N}t\right)-1\right])$, indicating that at the times $\tau_n = n\tau_{rec}^{(q)}$, $n = 0, 1, 2, \ldots$, periodic recurrences occur,

$$\tau_{rec}^{(q)} = \frac{2N\pi}{(j-k)q}\,. \tag{24}$$

We label this as the strong interaction recurrence time. The strong interaction decoherence time can be readily found by expanding the previous exponential at short times, yielding a Gaussian function of the form $e^{-t^2/2\tau_{dec}^2}$, from which we identify,

$$\tau_{dec}^{(q)} = \sqrt{\frac{N}{2}}\,\frac{\hbar}{q(j-k)\sin\theta}\,. \tag{25}$$

Note that both times $\tau_{rec}^{(q)}$ and $\tau_{dec}^{(q)}$ grow as does the number N of atoms that, as we discuss in the next section, appear as an "expected" feature of the thermodynamic behavior in the limit of a large number of atoms.

The diagonal terms $\rho_{jj}(t)$, for $j = -1, 0, +1$, are essentially constant equal to their initial values at $t = 0$. The precision of our calculations allows setting,

$$\rho_{jj}(t) \approx \rho_{jj}(0) + a_{jj}(\theta)e^{\frac{N}{2}\sin^2\theta\left[\cos\left(\frac{4q}{\hbar N}t\right)-1\right]}\,. \tag{26}$$

with $a_{jj}(\theta)$ a term that it is at most of the order of 10^{-9}, compared with the initial value $\rho_{kj}(0)$, for $N \lesssim 10^3$. The decoherence time scales as $\tau_{dec}^{(q)} \sim \sqrt{N}$ and the recurrence one $\tau_{rec}^{(q)} \sim N$, in agreement with this regime; see Equation (25).

In Figure 5, we show an example of the evolution of the density matrix in the strong interacting regime $q/N|\eta| \ll 1$ ($q = 1$, $p = 1$, and $\eta = -30000$ for $N = 700$). This illustrates both the typical behavior of decoherences and recurrences and the agreement with the heuristic fitting given by Equation (22). In Panels (a), (b), and (c), we show the evolution of the real part of the off-diagonal elements of the density matrix that show the sequence of decoherences followed by stationary states and recurrences. In Panel (d), we show the agreement with the predicted oscillations in terms of the q and p parameters.

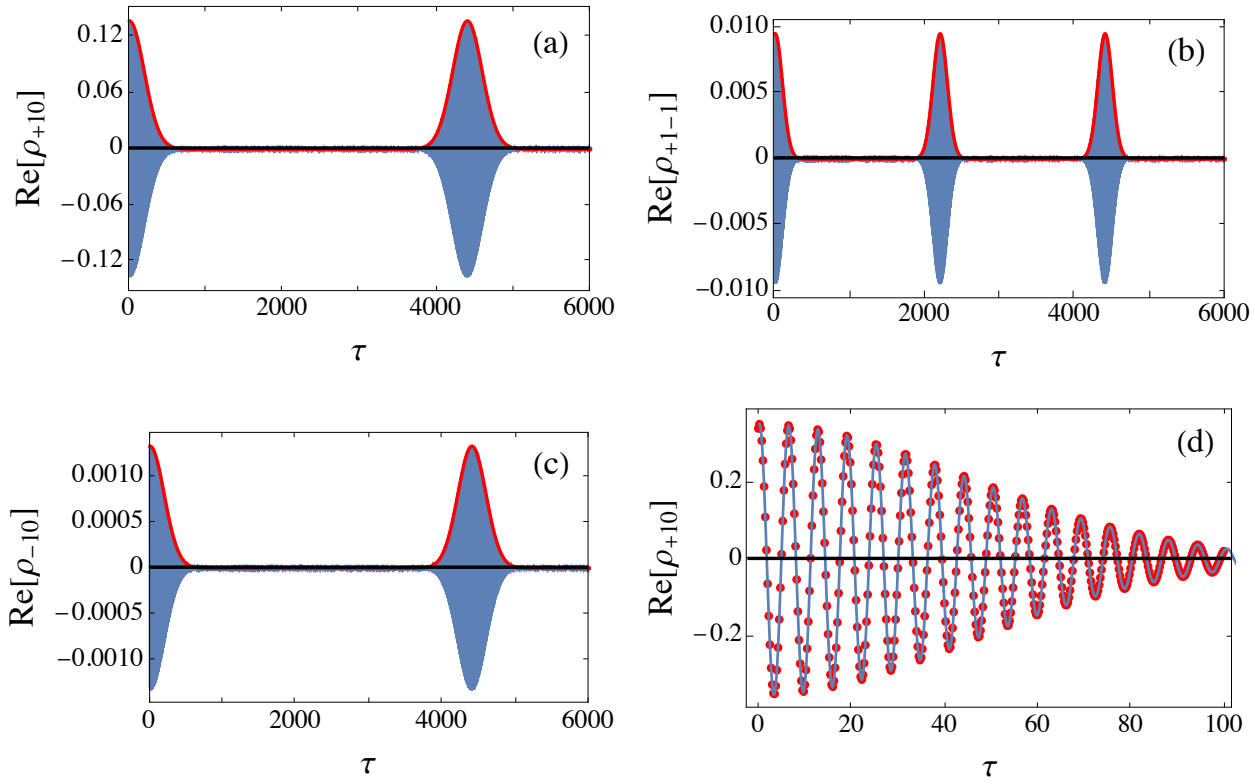

Figure 5. Real part of elements (**a**) $\rho_{+1,0}$, (**b**) $\rho_{+1,-1}$, and (**c**) $\rho_{-1,0}$ of the density matrix as a function of time, for $N = 700$, $q = 1$, $p = 1$, and $\eta = -30{,}000$, for a time period longer than $(0, 2\pi\hbar N/q)$. In continuous (red) lines, we show the overlap of the recurrences predicted by Equation (22). In Panel (**d**), we show an example of the agreement of the oscillations predicted by Equation (26), red dots, with the full quantum calculation, continuous blue line, for the real part of $\rho_{+1,0}$; $N = 1000$, $q = 1$, $p = 1$, and $\eta = 30{,}000$.

As shown in Figure 6 and confirmed by Equation (22), the behavior of one-body observables, such as $\langle \hat{f}_x \rangle$, shows a very detailed and predicted structure of decoherences and recurrences, with a stationary state for a very large parameter space. As seen in this and in all the above figures and expressions, the one-body density matrix of the stationary state is diagonal in the spin basis $(-1, 0, +1)$ along the z-direction. This physically means that while the expectation value of the z-component of the spin vector $\hat{\vec{f}}$, as well as the non-linear Zeeman term $\hat{Q}$ remain essentially constant, the x and y spin components decohere to zero. Note from the figure that if $q \ll 1$, but η finite, the recurrences can be separated by very long times that increase as N grows, thus yielding a true stationary state in the thermodynamic limit. To inquire into the nature of the stationary state, as illustrated in Figures 5 and 6 and in accord with Equations (22) and (26), we observe that the (quasi-)stationary one-body density matrix becomes diagonal with their diagonal terms numerically very close to the

initial ones. As suggested by ETH, we compute the average energy $\overline{E} = \langle\theta, \varphi|\hat{H}|\theta, \varphi\rangle$ and find the closest eigenenergy E_{M,m_M} of the system to such an average. We found in all studied cases for this regime that the corresponding stationary density matrix ρ_{jk} equals the density matrix $\rho_{jk}^{(s)}$ of the corresponding energy eigenstate $|M, m_M\rangle$; see Equation (14). Although we do not claim that the stationary state is thermal, this result agrees with the consequences of the eigenstate thermalization hypothesis. That is, all the one-body properties in the (quasi)stationary states are the same as if the system were in a true, exact, stationary energy eigenstate with the same eigenvalue as the average energy of the time-evolving system. As depicted in Figure 5, the recurrences become more separated as N increases, thus indicating that for a very large system, the quasistationary state cannot be distinguished from a true eigenstate, as far as measurable few-body properties are concerned. This is also along the explanation of thermalization in isolated many-body systems in statistical physics [18].

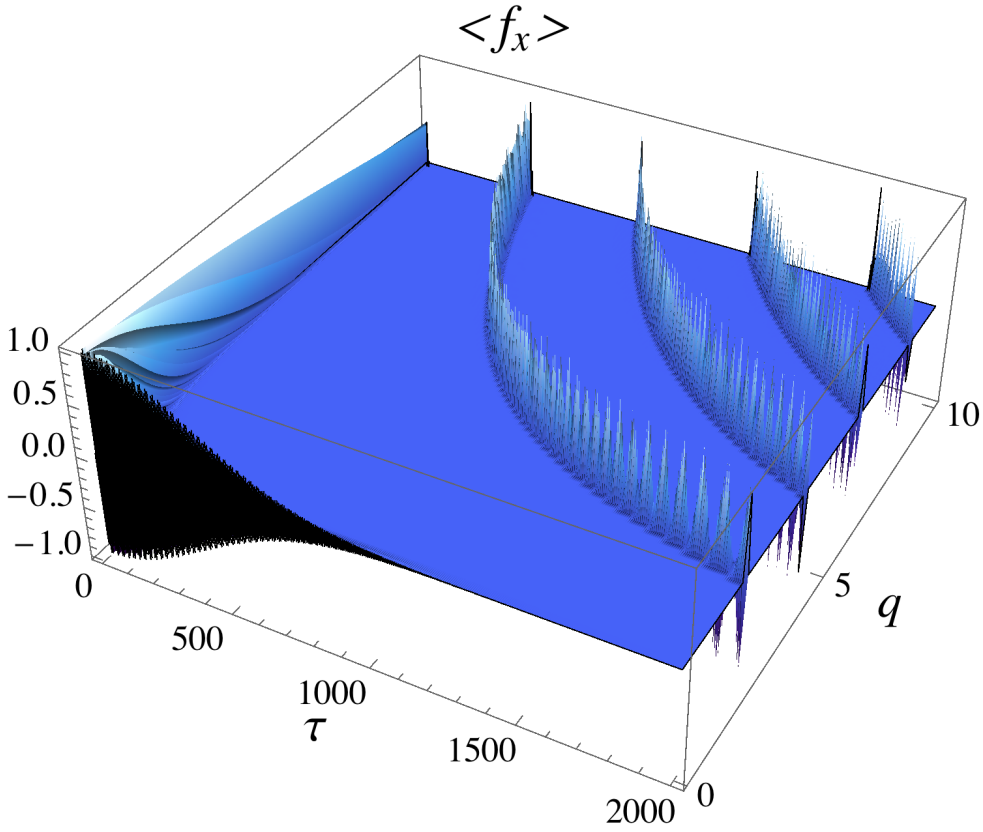

Figure 6. Evolution in time of the expectation value $\langle\hat{f}_x\rangle$ as a function of time τ and the non-linear Zeeman strength q, for $p = 1$ and $\eta = -30{,}000$. Note that if $q \ll 1$, the recurrences appear more separated.

4.2. Weak Interaction Regime $N|\eta|/q \ll 1$

Figure 7 shows the typical behavior of the elements of the one-body density matrix in the weak interaction regime, for a particular case; see the figure caption. We find that all essential features of the time evolution of the one-body reduced density matrix can be fitted quite well by the following explicit expressions.

$$\rho_{jk}(t) \approx \rho_{jk}(0) F_{jk}(N, \eta, \theta, t) e^{-2i(j-k)\eta N \cos\theta t} e^{-i(j-k)pt} e^{i\delta_{j,k\pm1}(\delta_{k,0}-\delta_{j,0})qt} \quad j \neq k \tag{27}$$

$$\rho_{jj}(t) \approx \rho_{jj}(0) + A_{jj}(\theta)\big(1 - F_{jj}(N, \eta, \theta, t)\big) \cos\frac{qt}{2} \tag{28}$$

where:

$$F_{jk}(N,\eta,\theta,t) = e^{g_{jk}(\theta)N\left(\cos(2f_{jk}\eta t)-1\right)} \quad \text{for all } j,k\,. \tag{29}$$

Above, $j,k=-1,0,+1$; f_{ij} are symmetrical with $f_{1,0}=1$, $f_{-1,1}=2$, $f_{-1,0}=3$ and all diagonal equal, $f_{jj}=4$. We were not able to find analytic expressions for the coefficients $g_{jk}(\theta)$ and $A_{jj}(\theta)$, but they can be numerically fitted, as we show them in Figures 8 and 9. The diagonal terms $g_{jj}(\theta)$ are all equal, shown in Figure 9. The initial condition is given again by the matrix in Equation (23).

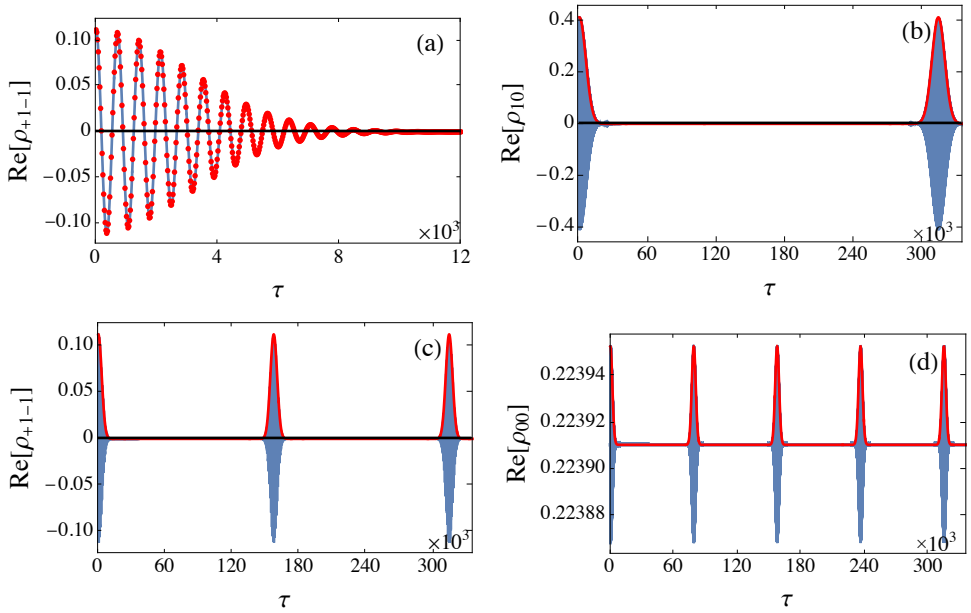

Figure 7. Real part of different elements of the density matrix as a function of time. (**a**) Comparison of the full quantum calculation (blue solid line) with heuristic fit (red dots), Equation (27), of $\rho_{+1,-1}$. Recurrences of the real parts of (**b**) $\rho_{+1,0}$, (**c**) $\rho_{+1,-1}$ and (**d**) $\rho_{0,0}$, within the time period $(0, 2\pi\hbar/\eta)$; the full quantum calculation (blue solid line) and overlap of heuristic fit (red line), Equation (27). The (dimensionless) parameters are $N=300$, $\eta=-10^{-5}$; $q=7$, $\theta=7\pi/30$, $p=0$, and $\varphi=0$.

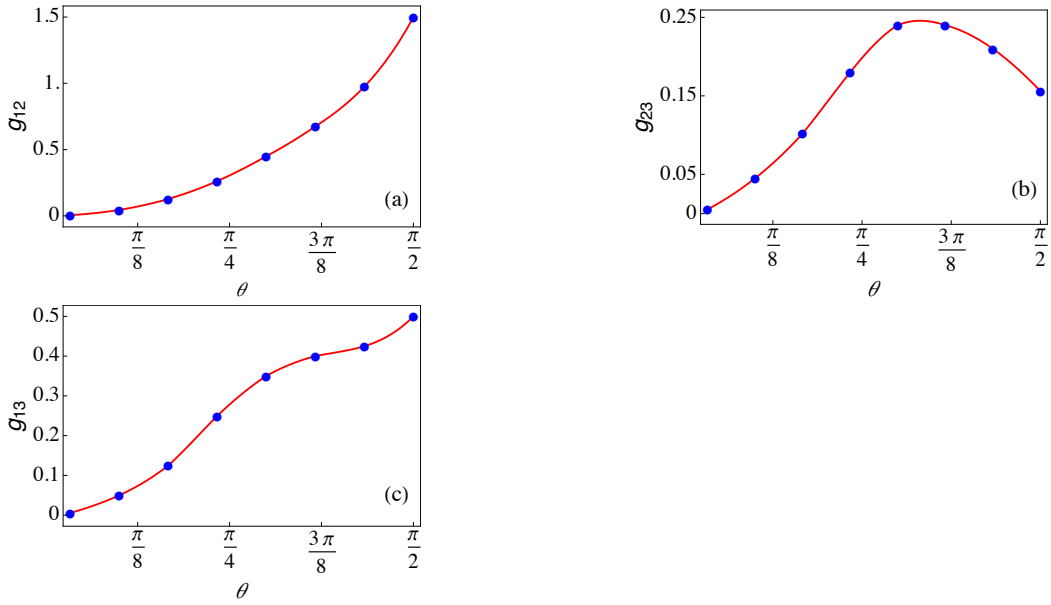

Figure 8. Coefficient $g_{jk}(\theta)$ as a function of θ, in Equation (29). (**a**) $g_{12}(\theta)$. (**b**) $g_{23}(\theta)$. (**c**) $g_{13}(\theta)$. The dots are values numerically calculated, and the continuous line is a spline interpolation. The parameters are $N=300$, $\eta=10^{-5}$; $q=7$, $p=0$, and $\varphi=0$.

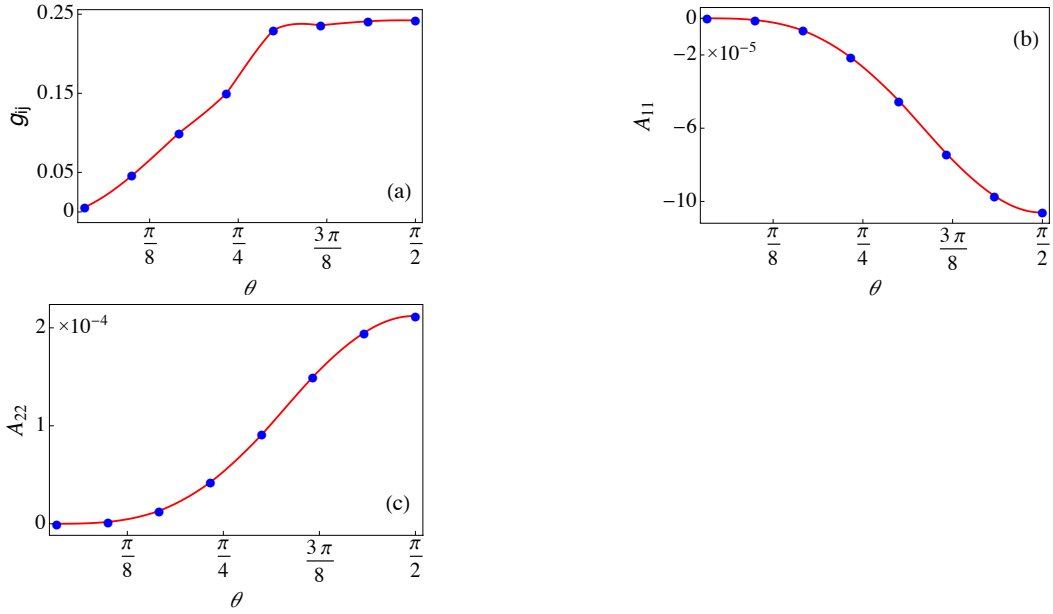

Figure 9. Amplitude coefficient (**a**) $A_{11}(\theta)$ and (**b**) $A_{22}(\theta)$ as a function of θ, in Equation (28). Note that both are very small. (**c**) Coefficient $g_{11}(\theta) = g_{22}(\theta) = g_{33}(\theta)$as a function of θ in Equation (29). The dots are values numerically calculated, and the continuous line is a spline interpolation. The parameters are $N = 300$, $\eta = 10^{-5}$; $q = 7$, $p = 0$, and $\varphi = 0$.

Figures 7 and 10 show the density matrix $\rho_{jk}(t)$ and the expectation value of the operator $\hat{f}_x$ for a single example in the limit $N|\eta|/q \ll 1$ ($\eta = -10^{-5}$ and $q = 7$, for $N = 300$). These figures illustrate the excellent agreement of the heuristic expression given by Equation (27) with the accurate numerical calculations. Figure 7a shows both cases for the initial decoherence, while Figure 7b–d the agreement in predicting the occurrence of the recurrences, for $\rho_{-1,0}$, $\rho_{-1,1}$, and $\rho_{0,0}$. Figure 10 shows the behavior of the elements (a) $\rho_{1,0}$ and (b) $\rho_{-1,0}$. As can be seen in Equation (27), these two elements oscillate with a very large frequency $q = 7$ and with a very small correction $\pm 2N\eta\cos\theta$, each taking one of the signs. This tiny difference between the oscillations of $\rho_{1,0}$ and (b) $\rho_{-1,0}$ shows itself in the beating pattern of the expectation value of $\hat{f}_x$ (see Equation (6)) shown in Figure 10c,d: the former is the exact numerical calculation and the latter the heuristic expression given by Equation (27). We found a quite remarkable agreement for any value of θ.

The behavior of intrinsic decoherences, followed by quasistationary states to further revivals or recurrences in a periodic fashion, is essentially contained in the function $F_{jk}(N,\eta,\theta,t) \approx e^{g_{jk}(\theta)N\left(\cos(2f_{jk}\eta t)-1\right)}$ within the density matrix; see Equation (27). The function F_{jk} indicates right away that there are recurrences at periodic intervals, $\tau_n = n\tau_{rec}$ with $n = 1, 2, 3, \ldots$, and:

$$\tau_{rec}^{(\eta)} = \frac{2\pi}{h_{j,k}|\eta|}\,, \tag{30}$$

that we label as the weakly interacting recurrence time; it depends on the particular matrix element, but the main point is its inverse proportionality to η and its independence on N. Then, at each recurrence, starting with the initial time $t = 0$, the evolution appears to decohere in a shorter time scale. This can be found by approximating the exponential for short times,

$$e^{g_{jk}(\theta)N\left(\cos(2f_{jk}\eta t)-1\right)} \approx e^{-g_{jk}(\theta)N\left(2f_{jk}\eta t\right)^2/2}\,, \tag{31}$$

thus identifying the weakly interacting decoherence time, $e^{-t^2/2\tau_{dec}^2}$,

$$\tau_{dec}^{(\eta)} = \sqrt{\frac{1}{g_{jk}(\theta)N}}\,\frac{\hbar}{2h_{jk}|\eta|}\,. \tag{32}$$

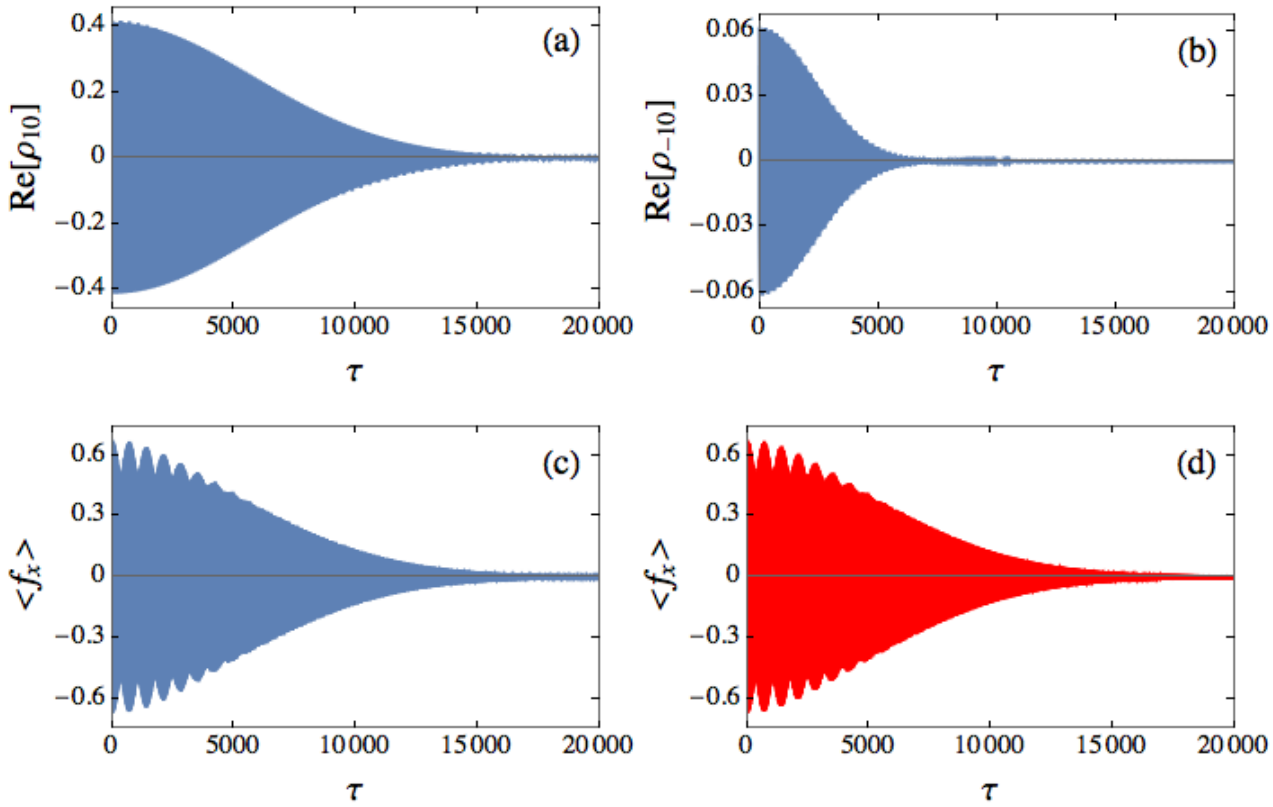

Figure 10. (**a**) Real part of element $\rho_{+1,0}$ of the density matrix as a function of time. (**b**) Real part of element $\rho_{-1,0}$ of the density matrix as a function of time. (**c**) Expectation value of $\hat{f}_x$ as a function of time, full quantum calculation; (**d**) expectation value of $\hat{f}_x$ as a function of time, heuristic fit, Equation (27). The beating pattern in $\langle \hat{f}_x(t) \rangle$ is due to the very small difference of the high frequency oscillations of between $\rho_{+1,0}$ and $\rho_{-1,0}$; see Equation (27). The parameters are $N = 300$, $\eta = -10^{-5}$; $q = 7$, $\theta = 7\pi/30$, $p = 0$, and $\varphi = 0$.

In this case, in addition to the dependence on η, there appears a dependence on the number N of atoms that is very different from the strong interaction case; see Equations (24) and (25). This is further discussed in the last section.

With regard to the (quasi)stationary states reached between consecutive recurrences or revivals, as shown in Figures 7 and 10 and verified in the expressions given by Equations (27)–(29), the off-diagonal terms of the reduced density matrix again vanish for time intervals during the (quasi)stationary state, with the diagonal terms becoming equal to the initial state. As in the strong interaction regime, since the energy eigenstate one-body density matrices (see Equation (14)) are also diagonal in the same spin basis, this suggests the same test of comparing the density matrices in the stationary regime of the coherent states with that of a true stationary eigenstate with the same average energy. Interestingly, contrary to the strong interacting regime, in this case, those do not agree. That is, the stationary state between recurrences does not seem to be a "true" stationary state, in the sense of ETH. This suggests, along the mentioned N dependence of the decoherence and recurrence times, that the weak regime is not typical of thermodynamic states. Although the full analysis of these stationary states is outside the scope of the present article, this indicates that the distribution of energy eigenstates in coherent states may show a more complex structure in the weak than in the strong limit.

5. Discussion and Final Remarks

The agreement between the proposed heuristic expressions for the time evolution of the one-body density matrix of an $F = 1$ SBEC, compared with (numerically) exact full quantum calculation is certainly quite good, allowing us to validate our conclusion that

those expressions are the leading non-trivial order, becoming better as N grows. Once more, in both cases, the general behavior shows periodic (intrinsic) decoherences of an oscillatory behavior, into stationary states, with periodic recurrences. However, the precise nature of this phenomenon is very different in the two limits considered. The most notorious difference between the extreme regimes resides on the fact that the role of the number of particles N is very different in each case. Note that in the weak side $\tau_{dec}^{(\eta)} \sim 1/\sqrt{N}$ and $\tau_{rec}^{(\eta)} \sim \mathcal{O}(1)$, while in the strong one $\tau_{dec}^{(q)} \sim \sqrt{N}$ and $\tau_{rec}^{(q)} \sim N$. It is of interest to mention that the non-linear single mode approximation, as described in [36,37], corresponds to the weak interaction regime. We find it relevant to recall that the validity of thermodynamics is achieved for macroscopic bodies $N \gg 1$. In this limit, the averages of extensive quantities scale as N while their fluctuations as $\sqrt{N}$ such that the ratio of deviations from equilibrium values scale as $1/\sqrt{N}$, hence tending to zero as N increases [18]. Moreover, the larger the system, the longer it takes to equilibrate in a stationary state, and the recurrences to initial states also are apart for a longer time. In this sense, it appears that the strong interacting regime fulfills this limit. That is, $\tau_{dec}^{(q)} \sim \sqrt{N}$ and $\tau_{rec}^{(q)} \sim N$ appear as reasonable results. More appealing is the fact that the ratio $\tau_{dec}/\tau_{rec} \sim 1/\sqrt{N}$, the mentioned typical condition for thermodynamic stability of a macroscopic system [18]. Thus, although both times diverge in the thermodynamic limit, at the appropriate scale, the decoherence time tends to zero as $\sim 1/\sqrt{N}$ compared to the recurrence one. Therefore, we find it very interesting to observe that while the decoherence and recurrence times in the weak interaction case, $N|\eta|/q \ll 1$, do not follow the "expected" thermodynamic trend, still we observe that the ratio $\tau_{dec}^{(\eta)}/\tau_{rec}^{(\eta)} \sim 1/\sqrt{N}$ scales appropriately. In any case, however, although the role of the number of atoms N is very different in each limit, still what is ultimately responsible for the decoherence and recurrence phenomena is the interaction among the constituents of the body. As we have also seen, this strong difference appears to be present in the structure of the stationary states attained between consecutive recurrences, having started in coherent states. As we verified, those stationary states are indistinguishable from true stationary energy eigenstates. The result that this property does not hold for a weakly interacting SBEC appears to be in agreement with the N dependence of the decoherence and recurrence times mentioned above. The full elucidation of these differences certainly deserves a separate and detailed study. In the crossover regime $N|\eta| \sim q$, both the interaction η and non-linear Zeeman q contributions compete, and their effect is intertwined, and even though the system indeed shows decoherences and recurrences, the latter no longer occurs at prescribed times depending on either $\sqrt{N}$ or N; see Figure 4c.

To summarize, we first highlight that one can exactly (numerically) diagonalize the Hamiltonian of an interacting $F = 1$ SBEC in the SMA approximation for a large number of atoms and that the method can be extended to larger spins $F > 1$. This allows us to probe the full quantum dynamics of any initial state. For the purposes of the present study, we chose here the relevant family of the coherent states. We studied the corresponding reduced one-body density matrix and found heuristic analytical expressions that fit remarkably well with its dynamics in the weak $N|\eta|/q \ll 1$ and strong $N|\eta|/q \gg 1$ regimes, indicating the interplay among the non-linear Zeeman effect $\sim q$ and the pairwise spin interaction $\sim \eta$, mediated by many-body effects $\sim N$. Our expressions predict the decoherence time and the recurrence periods in terms of these quantities and become more precise as N grows. Since the corresponding unitary propagator cannot be analytically found, due to its lack of closed Lie algebra, our results may indicate a path to find it in a series whose leading order term agrees with the heuristic expressions found here. A natural extension of the present study is the analysis of two-body correlations. For this, we need to calculate the reduced two-body density matrix, which with our method does not appear as a very difficult task. It would be very interesting to find how these correlations behave along the different regimes, to find out if the predicted decoherence and recurrence time hold, and it would also serve to further inquire into the structure and properties of the stationary state between recurrences.

Author Contributions: J.C.S.-S., R.P., and V.R.-R. contributed equally to this work. R.Z.-Z. collaborated in the initial stages of this work and in the solution of the GP equations. All authors read and agreed to the published version of the manuscript.

Funding: This work was partially funded by Grant IN108620 DGAPA (UNAM) and CONACYT 255573.

Acknowledgments: J.C.S.-S. acknowledges a postdoctoral scholarship at UNAM during the time this research was done.

Conflicts of Interest: The authors declare no conflict of interest.

References

1. Redfield, A. The theory of relaxation processes. In *Advances in Magnetic and Optical Resonance*; Academic Press: Cambridge, MA, USA, 1965; Volume 1, pp. 1–32.
2. Lindblad, G. On the generators of quantum dynamical semigroups. *Commun. Math. Phys.* **1976**, *48*, 119–130. [CrossRef]
3. Van Kampen, N.G. *Stochastic Processes in Physics and Chemistry*; Elsevier Science B.V.: Amsterdam, The Netherlands, 1992; Volume 1.
4. Van Kampen, N. A soluble model for quantum mechanical dissipation. *J. Stat. Phys.* **1995**, *78*, 299–310. [CrossRef]
5. Van Kampen, N. A new approach to noise in quantum mechanics. *J. Stat. Phys.* **2004**, *115*, 1057–1072. [CrossRef]
6. Hillery, M.; O'Connell, R.; Scully, M.; Wigner, E. Distribution functions in physics: Fundamentals. *Phys. Rep.* **1984**, *106*, 121. [CrossRef]
7. Zurek, W.H. Decoherence, einselection, and the quantum origins of the classical. *Rev. Mod. Phys.* **2003**, *75*, 715–775. [CrossRef]
8. Caldeira, A.O.; Leggett, A.J. Path integral approach to quantum Brownian motion. *Phys. A Stat. Mech. Appl.* **1983**, *121*, 587–616. [CrossRef]
9. Suárez, A.; Silbey, R.; Oppenheim, I. Memory effects in the relaxation of quantum open systems. *J. Chem. Phys.* **1992**, *97*, 5101–5107. [CrossRef]
10. Romero-Rochin, V.; Oppenheim, I. Relaxation properties of two-level systems in condensed phases. *Phys. A Stat. Mech. Appl.* **1989**, *155*, 52–72. [CrossRef]
11. Caballero-Benitez, S.F.; Romero-Rochín, V.; Paredes, R. Intrinsic decoherence in an ultracold Bose gas confined in a double-well potential. *J. Phys. B At. Mol. Opt. Phys.* **2010**, *43*, 095301. [CrossRef]
12. Camacho-Guardian, A.; Paredes, R. Intrinsic decoherence and purity in a Bose quantum fluid in a triple well potential. *Laser Phys.* **2014**, *24*, 085501. [CrossRef]
13. Engel, G.S.; Calhoun, T.R.; Read, E.L.; Ahn, T.K.; Mančal, T.; Cheng, Y.C.; Blankenship, R.E.; Fleming, G.R. Evidence for wavelike energy transfer through quantum coherence in photosynthetic systems. *Nature* **2007**, *446*, 782–786. [CrossRef] [PubMed]
14. Collini, E.; Wong, C.Y.; Wilk, K.E.; Curmi, P.M.; Brumer, P.; Scholes, G.D. Coherently wired light-harvesting in photosynthetic marine algae at ambient temperature. *Nature* **2010**, *463*, 644–647. [CrossRef] [PubMed]
15. Marques, B.; Matoso, A.; Pimenta, W.; Gutiérrez-Esparza, A.; Santos, M.; Pádua, S. Experimental simulation of decoherence in photonics qudits. *Sci. Rep.* **2015**, *5*, 16049. [CrossRef] [PubMed]
16. Ballmann, S.; Härtle, R.; Coto, P.B.; Elbing, M.; Mayor, M.; Bryce, M.R.; Thoss, M.; Weber, H.B. Experimental evidence for quantum interference and vibrationally induced decoherence in single-molecule junctions. *Phys. Rev. Lett.* **2012**, *109*, 056801. [CrossRef]
17. Gu, B.; Franco, I. Quantifying early time quantum decoherence dynamics through fluctuations. *J. Phys. Chem. Lett.* **2017**, *8*, 4289–4294. [CrossRef]
18. Landau, L.; Lifshitz, E. *Statistical Physics I*; Pergamon Press: Oxford, UK; London, UK; Edinburgh, UK; New York, NY, USA; Paris, France; Frankfurt, Germany, 1980.
19. Anderson, M.H.; Ensher, J.R.; Matthews, M.R.; Wieman, C.E.; Cornell, E.A. Observation of Bose–Einstein Condensation in a Dilute Atomic Vapor. *Science* **1995**, *269*, 198–201. [CrossRef]
20. Davis, K.B.; Mewes, M.O.; Andrews, M.R.; van Druten, N.J.; Durfee, D.S.; Kurn, D.M.; Ketterle, W. Bose–Einstein Condensation in a Gas of Sodium Atoms. *Phys. Rev. Lett.* **1995**, *75*, 3969–3973. [CrossRef]
21. Regal, C.A.; Greiner, M.; Jin, D.S. Observation of Resonance Condensation of Fermionic Atom Pairs. *Phys. Rev. Lett.* **2004**, *92*, 040403. [CrossRef]
22. Vinit, A.; Raman, C. Precise measurements on a quantum phase transition in antiferromagnetic spinor Bose–Einstein condensates. *Phys. Rev. A* **2017**, *95*, 011603. [CrossRef]
23. Gomez, P.; Mazzinghi, C.; Martin, F.; Coop, S.; Palacios, S.; Mitchell, M.W. Interferometric measurement of interhyperfine scattering lengths in ^{87}Rb. *Phys. Rev. A* **2019**, *100*, 032704. [CrossRef]
24. Gomez, P.; Martin, F.; Mazzinghi, C.; Benedicto Orenes, D.; Palacios, S.; Mitchell, M.W. Bose–Einstein Condensate Comagnetometer. *Phys. Rev. Lett.* **2020**, *124*, 170401. [CrossRef] [PubMed]
25. Ketterle W.; Durfee, D.S.; Stamper-Kurn, D.M. Making, probing and understanding Bose–Einstein condensates. In *Proceedings of the International School of Physics "Enrico Fermi"*; Inguscio, S.M., Stringari, C.W., Eds.; IOS Press EBooks: Amsterdam, The Netherlands, 1999; Volume 140, pp. 67–176.

26. Deutsch, J.M. Quantum statistical mechanics in a closed system. *Phys. Rev. A* **1991**, *43*, 2046–2049. [CrossRef] [PubMed]
27. Srednicki, M. Chaos and quantum thermalization. *Phys. Rev. E* **1994**, *50*, 888–901. [CrossRef] [PubMed]
28. Rigol, M.; Dunjko, V.; Olshanii, M. Thermalization and its mechanism for generic isolated quantum systems. *Nature* **2008**, *452*, 854–858. [CrossRef] [PubMed]
29. Reimann, P. Canonical thermalization. *New J. Phys.* **2010**, *12*, 055027. [CrossRef]
30. Kaufman, A.M.; Tai, M.E.; Lukin, A.; Rispoli, M.; Schittko, R.; Preiss, P.M.; Greiner, M. Quantum thermalization through entanglement in an isolated many-body system. *Science* **2016**, *353*, 794–800. [CrossRef]
31. Choi, J.y.; Hild, S.; Zeiher, J.; Schauß, P.; Rubio-Abadal, A.; Yefsah, T.; Khemani, V.; Huse, D.A.; Bloch, I.; Gross, C. Exploring the many-body localization transition in two dimensions. *Science* **2016**, *352*, 1547–1552. [CrossRef]
32. Ho, T.L. Spinor Bose condensates in optical traps. *Phys. Rev. Lett.* **1998**, *81*, 742. [CrossRef]
33. Ohmi, T.; Machida, K. Bose–Einstein Condensation with Internal Degrees of Freedom in Alkali Atom Gases. *J. Phys. Soc. Jpn.* **1998**, *67*, 1822–1825. [CrossRef]
34. Damski, B.; Zurek, W.H. Quantum phase transition in space in a ferromagnetic spin-1 Bose–Einstein condensate. *New J. Phys.* **2009**, *11*, 063014. [CrossRef]
35. Kajtoch, D.; Witkowska, E. Spin squeezing in dipolar spinor condensates. *Phys. Rev. A* **2016**, *93*, 023627. [CrossRef]
36. Imamoğlu, A.; Lewenstein, M.; You, L. Inhibition of Coherence in Trapped Bose–Einstein Condensates. *Phys. Rev. Lett.* **1997**, *78*, 2511–2514. [CrossRef]
37. Plimak, L.; Weiß, C.; Walser, R.; Schleich, W.P. Quantum dynamics of atomic coherence in a spin-1 condensate: Mean-field versus many-body simulation. *Opt. Commun.* **2006**, *264*, 311–320. [CrossRef]
38. Zamora-Zamora, R.; Romero-Rochín, V. Skyrmions with arbitrary topological charges in spinor Bose–Einstein condensates. *J. Phys. B At. Mol. Opt. Phys.* **2018**, *51*, 045301. [CrossRef]
39. Zamora-Zamora, R.; Domínguez-Castro, G.A.; Trallero-Giner, C.; Paredes, R.; Romero-Rochín, V. Validity of Gross–Pitaevskii solutions of harmonically confined BEC gases in reduced dimensions. *J. Phys. Commun.* **2019**, *3*, 085003. [CrossRef]
40. Xue, M.; Yin, S.; You, L. Universal driven critical dynamics across a quantum phase transition in ferromagnetic spinor atomic Bose–Einstein condensates. *Phys. Rev. A* **2018**, *98*, 013619. [CrossRef]
41. Law, C.; Pu, H.; Bigelow, N. Quantum spins mixing in spinor Bose–Einstein condensates. *Phys. Rev. Lett.* **1998**, *81*, 5257. [CrossRef]
42. Pu, H.; Law, C.; Raghavan, S.; Eberly, J.; Bigelow, N. Spin-mixing dynamics of a spinor Bose–Einstein condensate. *Phys. Rev. A* **1999**, *60*, 1463. [CrossRef]
43. De Sarlo, L.; Shao, L.; Corre, V.; Zibold, T.; Jacob, D.; Dalibard, J.; Gerbier, F. Spin fragmentation of Bose–Einstein condensates with antiferromagnetic interactions. *New J. Phys.* **2013**, *15*, 113039. [CrossRef]
44. Koashi, M.; Ueda, M. Exact eigenstates and magnetic response of spin-1 and spin-2 Bose–Einstein condensates. *Phys. Rev. Lett.* **2000**, *84*, 1066. [CrossRef]
45. Santos, L.; Pfau, T. Spin-3 chromium bose-einstein condensates. *Phys. Rev. Lett.* **2006**, *96*, 190404. [CrossRef] [PubMed]
46. Raghavan, S.; Pu, H.; Law, C.; Bigelow, N. Properties of spinor Bose condensates. *J. Low Temp. Phys.* **2000**, *119*, 437–460. [CrossRef]
47. Bookjans, E.M.; Vinit, A.; Raman, C. Quantum phase transition in an antiferromagnetic spinor Bose–Einstein condensate. *Phys. Rev. Lett.* **2011**, *107*, 195306. [CrossRef] [PubMed]
48. Dağ, C.B.; Wang, S.T.; Duan, L.M. Classification of quench-dynamical behaviors in spinor condensates. *Phys. Rev. A* **2018**, *97*, 023603. [CrossRef]
49. Anquez, M.; Robbins, B.; Bharath, H.; Boguslawski, M.; Hoang, T.; Chapman, M. Quantum Kibble-Zurek mechanism in a spin-1 Bose–Einstein condensate. *Phys. Rev. Lett.* **2016**, *116*, 155301. [CrossRef] [PubMed]
50. Gell-Mann, M. Symmetries of Baryons and Mesons. *Phys. Rev.* **1962**, *125*, 1067–1084. [CrossRef]
51. Cohen-Tannoudji, C.; Diu, B.; Laloe, F. *Quantum Mechanics*; John Wiley and Sons: New York, NY, USA, 1977; Volume I.
52. Sandoval-Santana, J.C.; Ibarra-Sierra, V.G.; Cardoso, J.L.; Kunold, A.; Roman-Taboada, P.; Naumis, G. Method for Finding the Exact Effective Hamiltonian of Time-Driven Quantum Systems. *Ann. Phys.* **2019**, *531*, 1900035. [CrossRef]